Singlet-oxygen-driven photocatalytic degradation of gaseous formaldehyde and its mechanistic study

Su Keun Kuk [1], Sang Min Ji [1], Sungwoo Kang, Dong Sik Yang, Hyuk Jae Kwon, Min Seok Koo, Sehyeong Oh, Hyun Chul Lee [*]

Samsung Advanced Institute of Technology, Samsung Electronics Co., Ltd, 130 Samsung-ro, Yeongtong-gu, Suwon-si, Gyeonggi-do 16678, the Republic of Korea

ARTICLE INFO

ABSTRACT

Conventional studies on photocatalytic oxidation reaction have focused primarily on hydroxyl radical (•OH) as a major reactive oxygen species (ROS). This perspective may not be suitable for gaseous HCHO photodegradation due to the short lifetime and diffusion length of •OH. Identification of divergent ROS and understanding their characteristics for the gas-phase photocatalytic oxidation are further required. Here, we report a BiOI/TiO$_2$ p-n junction photocatalyst, which uses mobile singlet oxygen ($^1O_2$) as the main ROS for gaseous HCHO photooxidation. The introduction of p-n heterojunctions causes a charge transfer that prefers mobile $^1O_2$ generation rather than •OH due to an energetically favorable desorption free energy, accelerating HCHO oxidation. Finally, we demonstrated the photocatalytic filter performance of HCHO-to-CO$_2$ conversion for 150 h with a conversion efficiency of 87 ± 1.3 % in a single-pass reactor. Our systematic study reveals the potential of the overlooked $^1O_2$-driven gaseous HCHO photocatalytic degradation process.

1. Introduction

Photocatalytic oxidation is a promising method for removing gas-phase volatile organic compounds (VOCs), such as formaldehyde (HCHO), implicated in health problems like irritation and tumors [1–3]. Photocatalytic degradation involves the formation of reactive oxygen species (ROS) to oxidize and degrade HCHO [4]. The hydroxyl radical (•OH) is a highly active ROS [5] and is regarded as the most effective ROS for photocatalytic HCHO decomposition [6]. However, due to its short lifetime ($\sim$ 20 ms) and diffusion length ($<$ 1 mm) in the gas phase, most •OH formed on the surface of photocatalysts reacts with adsorbed organic compounds rather than diffusing into the air to react with gaseous VOC [7]. Thus, •OH-driven photocatalytic gaseous VOC degradation merits re-examination [8]. More research on ROS formation conditions and their role in photocatalytic reactions is required to identify divergent ROS like superoxide radical (•O$_2^-$) and singlet oxygen ($^1O_2$) and understand their characteristics for photocatalytic oxidation in gas-phase reaction [9].

Previous studies have rarely considered using ROS other than •OH, such as •O$_2^-$ and $^1O_2$, for the photocatalytic degradation of gaseous VOC [10,11]. Different oxidants may be key to gaseous HCHO

photodegradation in various condition due to the difference in properties such as lifetime, diffusion length, and energy (Table S1). $^1O_2$, derived from O$_2$, is a non-radical and non-ionic oxygen species in its lowest excited electronic state; it can diffuse freely to the air ($\sim$ 1 cm), has a long lifetime ($\sim$ 2 s), and robustly reacts with reactants [12,13]. $^1O_2$ can rapidly react with electron-rich moieties in organic compounds due to the higher energy (95 kJ mol^{-1}) than the ground state of oxygen [14]. Therefore, it has previously been reported that $^1O_2$ can enhance selective oxidation of gas-phase VOCs such as dioxin-like compounds, furans, and NO$_x$ [15–17]. However, in photocatalytic oxidation, most studies have considered $^1O_2$ as a minor ROS. Under the low humidity condition, the quenching of gaseous $^1O_2$ by airborne water is minimized, and $^1O_2$ can be used as a substitute for •OH as a major ROS [8]. Further research on $^1O_2$-driven photocatalytic degradation of gaseous HCHO is necessary, particularly monitoring and mechanistic studies of $^1O_2$ generation and its role in HCHO oxidation.

Herein we present a p-n junction photocatalyst, BiOI/TiO$_2$, which uses mobile $^1O_2$ as the main ROS for gaseous HCHO photocatalytic degradation. By spectroscopic analyses and radical monitoring, we confirmed that the introduction of p-n heterojunctions causes a built-in internal electric field inducing fast charge transfer, thus promoting the

generation of mobile $^1O_2$ instead of •OH. Density functional theory (DFT) calculations revealed enhanced the generation of $^1O_2$ via energetically favored desorption free energy, resulting in the acceleration of HCHO oxidation. We also performed in-situ spectroscopic studies to understand the reaction mechanism involving the reactive $^1O_2$. To the best of our knowledge, it is the first report about $^1O_2$-driven HCHO photodegradation in the gas phase. Finally, we integrated the BiOI/TiO$_2$ photocatalyst with a honeycomb-type particulate filter, and demonstrated $^1O_2$-driven robust photocatalytic HCHO degradation process in a single-pass reactor.

2. Experimental

2.1. Synthesis of catalysts

The BiOI/TiO$_2$ (10 wt% BiOI) composite was prepared by one-pot chemical bath synthesis (denoted as BTO, BiOI-TiO$_2$ composite by One-pot synthesis). Briefly, 1.45 g of Bi(NO$_3$)$_3$·5 H$_2$O (99.99 %, trace metals basis, Sigma-Aldrich) was dissolved in 180 ml of 1.8 M acetic acid (99.7 %, ACS reagent, Sigma-Aldrich) solution. Then 9.5 g of TiO$_2$ (80 % anatase crystallinity ST-01, Ishihara Inc.) was added to the Bi precursor containing solution (Solution A). Meanwhile, 0.50 g of KI (99.5 %, BioUltra, Sigma-Aldrich) was added to 30 ml deionized (DI) water (Solution B). After 30 min stirring with a rotational speed of 500 rpm and 30 min sonication for each solution, solution B was slowly drop-wised into the solution A with continuous magnetic stirring. The mixture solution was stirred for 2 h and the resulting material was collected by centrifugation. The obtained BTO powder was washed with DI water several times and dried under vacuum conditions at 80 °C overnight. To remove remaining carbon sources, collected composites were annealed at 200 °C in air for 3 h with a heating ramp rate of 5 °C min^{-1} using a muffle furnace. For preparation of BiOI-TiO$_2$ composite by Mixing (BTM) as a comparative sample, BiOI was synthesized by a chemical precipitation method according to the previous report [18]. 9 g TiO$_2$ and 1 g BiOI (9:1 wt/wt) were mixed in 180 ml of DI water by physical mixing. After 1 h sonication and 3 h magnetic stirring at 500 rpm, the resulted solution was transferred to a rotary evaporator equipped with a water bath set to 90 °C and a vacuum pump. The solvent was removed under vacuum condition with a rotation speed of 100 rpm. The final BTM powder was collected and slightly ground by mortar.

2.2. Material characterization

The morphology of the photocatalysts was observed using scanning electron microscopy (SEM, SU-8030, Hitachi) and high-resolution transmission electron microscopy (HR-TEM, Titan G2, FEI). X-ray diffraction (XRD) patterns of catalysts were measured using an X-ray diffractometer (D8 Advance, Bruker) with Cu Kα radiation (λ = 0.154 nm). X-ray photoelectron spectroscopy (XPS, Quantum 2000, Physical Electronics) was used to confirm the chemical states of composites with Al Kα photon source. All peak positions were calibrated with the C 1 s peak (285 eV) as a reference. The UV–visible spectra of catalyst powders were recorded using a UV–visible spectrophotometer equipped with a diffuse reflectance attachment (Solidspec-3700, Shimadzu) in which BaSO$_4$ was employed as a reflectance standard. Photoluminescence (PL, Fluromax, Horiba) for evaluating charge recombination rate of photocatalysts was also conducted under excitation wavelength of 310 nm. The catalyst was characterized using Brunauer–Emmett–Teller (BET, BELSORP-max, BEL) for surface area measurement. Photocurrent density, electrochemical impedance spectroscopy (EIS) Nyquist plot and Mott–Schottky plot were conducted by potentiostat (WMPG 1000, Wonatech). All photoelectrochemical measurements were recorded with a single cell compartment in a three-electrode configuration (an Ag/AgCl reference electrode in 3 M NaCl and a Pt wire counter electrode). For electrode preparation, 20 µl of photocatalysts (1 mg ml^{-1} in ethanol) was drop-casted on a washed fluorine-doped tin oxide (FTO) glass

electrode and dried completely at 80 °C. The 0.1 M phosphate buffer solution (pH 7) was used for experiments.

2.3. HCHO photodegradation test

HCHO Photocatalytic degradation test was conducted in a single-pass continuous flow reactor. The photocatalysts were located under a quartz window. HCHO was supplied via the vaporization of para-formaldehyde (95 %, Sigma-Aldrich) powder with a carrier gas of N$_2$. The measurement of HCHO and CO$_2$ concentration was conducted by the real time gas analysis FT-IR spectrometer (Titan I4001-E, MIDAC). A gaseous mixture of 500 ml min^{-1} synthetic air (20 % O$_2$ balance 80 % N$_2$) containing 20 ppmv HCHO with a designated humidity was fed to the reactor. The customized reactor is an airtight reactor with a tetragonal inner space (2.6 × 5 × 1 cm^3), and the sample holder (Effective area of 2 × 2 cm^2) is firmly inserted into this inner space. The sample (100 mg) in the reactor was illuminated by a 365 nm UV LED (Fiber Optics Korea Co) with a light intensity of 50 mW cm^{-2} (4 cm^2, illuminated area).

2.4. Rate constant calculations

The photoconversion (%), residence time (s) and conversion rate constant (k_c, s^{-1}) for HCHO photoconversion to CO$_2$ were derived using the Eqs. (1), (2), and (3), respectively.

$$X_{HCHO} = \frac{C_{CO_2}}{C_{HCHO}} \times 100\ \% \tag{1}$$

$$\tau = \frac{V}{F} = \frac{S \times \delta}{F} \tag{2}$$

$$k_c = \frac{-\ln(1 - X_{HCHO})}{\tau} \tag{3}$$

where C$_{CO2}$ and C$_{HCHO}$ represent the concentrations of CO$_2$ in outlet gas and formaldehyde in inlet gas (ppmv), respectively. The symbols V, F, S, δ represent the effective volume of the reactor (cm^3), flow rate (8.33 cm^3 s^{-1}), effective area of the catalyst (4 cm^2), and the gap distance between the sample and the quartz window (0.65 cm), respectively.

The photodegradation rate constant (k_d, min^{-1}) for intermediate degradation during HCHO photoconversion to CO$_2$ was derived using the Eq. (4).

$$k_d = \frac{-\ln(I/I_0)}{t} \tag{4}$$

where I$_0$ and I are the initial and instantaneous intensities of intermediates in in-situ diffuse reflectance infrared Fourier transform spectroscopy (DRIFTS) analysis, respectively. t (min^{-1}) is the reaction time of DRIFTSTS analysis.

2.5. ROS monitoring

The ROS were monitored by electron paramagnetic resonance (EPR) spectrometer (EMX plus, Bruker) equipped with dual mode DM1012 resonator at 9.64 GHz. 5,5-dimethyl-1-pyrroline-N-oxide (DMPO, 98 %, Supelco) and 2,2,6,6-tetramethylpiperidine (TEMP, 99 %, Sigma-Aldrich) were used as spin-trapping agents for •OH and $^1O_2$, respectively. Briefly, the photocatalyst was dispersed in spin trapping solution with a concentration of 2 mg ml^{-1} (5 mg). The concentrations for the trapping solution were 350 mM for DMPO and 240 mM for TEMP. For •O$_2^-$ trapping, methanol (99.5 %, Samchun) was added into the DMPO solution to avoid the interference of •OH. The solution was irradiated under 365 nm UV light for 10 min and the resulting suspension was filtered through a 0.22 µm Micron syringe filter. All spectra were acquired with microwave power of 3 mW, modulation amplitude of 1.0 G, and modulation frequency of 100 kHz. For identification of intermediate

radical during HCHO degradation, additional formaldehyde solution (37 wt%, Sigma-Aldrich) was also introduced into the trapping solution (9:1 v/v).

·OH monitoring was also conducted by PL using terephthalic acid (TA, 98 %, Sigma-Aldrich). 0.5 mg ml^{-1} of photocatalyst was dispersed in 2 mM NaOH solution in the presence of 500 µM of TA. Under magnetic stirring, 365-nm UV light was irradiated to the solution. PL peak of 2-hydroxyterephthalic acid (HTA), which produced from reaction of TA with the ●OH, at 425 nm was observed after the reaction.

To further explore $^1O_2$ generation pathway, furfuryl alcohol (FFA, 98 %, TOKCHE) was used as a trapping chemical for $^1O_2$. 4 ml of aqueous solutions containing 100 µM FFA was prepared. Then 4 mg of BTO was added into the solution. After stirring in the dark for 30 min, experiment conducted under 365 nm UV LED with a light intensity of 50 mW cm^{-2}. For quenching test, 100 mM of triethanolamine (TEOA, 99 %, Sigma-Aldrich) was added into the solution as a hole scavenger. The resulting solution was filtered through a 0.22 µm Micron syringe filter and analyzed by a high-performance liquid chromatography (HPLC, e2695, Waters) with a Supelco LC-18 column and a UV-Visible detector. The flow rate of eluent (DI water: Acetonitrile (99.9 % Samchun), 9:1 v/v) was 0.5 ml min^{-1}.

2.6. Mobile $^1O_2$ monitoring

The experimental set-up for mobile $^1O_2$ monitoring employed involved photocatalysts and hydrophobic quartz wool in the quartz column. The O_2 gas was delivered through a quartz column to the surface of the solution containing 15 mg of photocatalysts at a flow rate of 120 ml min^{-1}. 4 ml of 100 µM FFA solution was used as a trapping solution for mobile $^1O_2$. The distance between photocatalysts and the trapping solution was 0.5 cm. The sample in the reactor was illuminated by a 365 nm UV LED with a light intensity of 50 mW cm^{-2}. FFA and 6-hydroxy-(2 H)-pyran-3-one (6 HP-one), a product chemical from the reaction between FFA and $^1O_2$, were measured using the HPLC. The concentration of 6-HP-one (97 % BLDPHA) was calibrated before mobile $^1O_2$ monitoring test.

2.7. In-situ DRIFTS analyses

HCHO photodegradation on the photocatalyst surface was monitored by in-situ DRIFTS (Nicolet iS50 FTIR, Thermo Fisher) equipped with an in-situ diffuse-reflectance cell (Harrick). To analyze the intermediates during HCHO photodegradation, 50 mg of photocatalyst was loaded under a synthetic gas air (200 ml min^{-1}) with 365 nm UV lamp irradiation. Before measurements, prepared samples were pretreated 1 h at 120 °C to remove the adsorbed species on the catalyst surface.

2.8. Photocatalytic filter preparation and test

For photocatalytic filter preparation, photocatalyst was loaded on a honeycomb-type particulate filter monolith (3.8 × 3.8 ×6 cm^3 ceramic filter, 200 cells per in^2 (CPSI)) by wash-coating method. Before loading, the monolith was washed with acetone and ethanol under 30 min sonication and dried at 80 °C for 12 h. For coating solution, 20 g of BTO sample was dispersed in 180 ml of DI water (1:9 wt/wt). After 1 h sonication and 3 h magnetic stirring at 500 rpm, the monolith was dipcoated in the solution. The excess solution was blown off using compressed air. Then, the photocatalytic filter was dried at 80 °C for 4 h. The coating method was repeated to reach the catalyst coating amount (43.6 g$_{cat}$ L^{-1}). For photocatalytic filter test, the customized Teflon reactor was equipped with an optical polished quartz window at a total gas flow rate of 10 L min^{-1} (20 ppmv HCHO) under UV light irradiation. The reactor is a cylinder-type reactor with a tetragonal inner space (4.2 × 4.2 × 12 cm^3), and the filter was air-tightly fitted.

3. Results and discussion

3.1. Materials synthesis and characterization

We fabricated BTO photocatalyst by the one-pot synthesis method. For comparison, BTM was prepared by physically mixing of TiO_2 and BiOI in an aqueous solution. We used SEM to investigate the BTO morphology. Fig. 1a shows that BTO formed a composite of TiO_2 and BiOI with a size of 1.4 ± 0.3 µm average diameter. By contrast in BTM, BiOI and TiO_2 existed individually, not fully integrated, indicating less interfacial contact between BiOI and TiO_2 (Figs. S1, S2). X-ray diffraction (XRD) patterns revealed a composite phase structure (Fig. S3), with strong diffraction peaks indicating the presence of BiOI (JCPDS card no. 10–0445) and TiO_2 (JCPDS card no. 21–1272) crystal phases. HR-TEM and fast Fourier transform (FFT) pattern analysis of the BTO catalyst were performed to investigate the crystal structure (Fig. 1b), revealing ordered lattice fringes and spots corresponding to the (101) plane of TiO_2 and (102) plane of BiOI, consistent with the XRD results. Scanning transmission electron microscopy combined with energy-dispersive X-ray spectroscopy (STEM-EDS) elemental mapping demonstrated that the constituent elements Bi, Ti, and O were homogeneously distributed in the composite (Fig. 1c). Thus, we concluded that the BTO was successfully fabricated with extensive interfacial contacts between BiOI and TiO_2.

XPS was used to compare the chemical states of elements in the photocatalysts (TiO_2, BiOI, BTM, and BTO) (Fig. 1d-f and Fig. S4). The Ti 2p spectra indicate that the titanium is in the Ti^{4+} form in TiO_2 [19]. The binding energies of Bi 4 f and I 3d spectra correspond to Bi^{3+} and I$^-$ in BiOI, respectively. Interestingly, significantly higher shifts in the Ti 2p, Bi 4 f, and I 3d were detected in BTO compared to BTM, demonstrating alterations in the elemental binding energies and chemical environments. The characteristic Ti 2p spectral peaks shifted higher binding energies, while those in the Bi 4 f and I 3d spectra shifted lower binding energies. We attribute that these shifts are due to the strong electronic interaction between TiO_2 and BiOI [20,21]. The electronegativity difference between Ti (1.54) in TiO_2 and Bi (2.02) and I (2.66) in BiOI induces favorable charge transfer. The O 1 s spectra were deconvoluted into two peaks assigned to the Ti-O bond (530.2 eV) and oxygen vacancy (O_v, 531.3 eV). Oxygen vacancies can be generated during heterojunction construction in composites [22]. The peak area percentage gives the contents of Ti-O bond and O_v in O 1 s spectra (Table S2). The percentage of O_v of BTO is 40%, which is higher than that of BTM (29.9 %). This implies that BTO possesses more interfacial junctions for charge transfer than BTM.

3.2. Spectroscopic analyses and HCHO photodegradation performance

We conducted several spectroscopic analyses to explore the charge transfer of photo-induced electron-hole pairs in the composites. The UV–Vis diffuse reflectance spectra of the photocatalysts are presented in Fig. S5a. The TiO_2 and BiOI band gaps were determined from the Tauc plot as 3.23 and 1.88 eV, respectively (Fig. S5b). The UV–Vis spectra of BTM and BTO displayed an enhanced absorption band compared to TiO_2. Absorbance at 365 nm was strongly enhanced for BTO compared to BTM. It has been reported that inhibited photoelectron-hole recombination could result in a strong response in light absorption [23]. The PL spectra (Fig. 1 g) had a PL emission peak around 375 nm when the photo-generated carriers recombined in TiO_2. After the heterojunction, the BiOI/TiO_2 composite showed decreased PL compared to TiO_2, demonstrating less charge recombination because of the charge separation in the composites. BTO showed lower PL than BTM, demonstrating that more heterojunctions necessary for charge separation were formed between the BiOI and TiO_2 in BTO.

EIS Nyquist plots (Fig. S5c) show that, among the photocatalysts studied, BTO has the smallest charge transfer resistance (80.0 kΩ) under UV light irradiation. This indicates faster interfacial transfer kinetics for
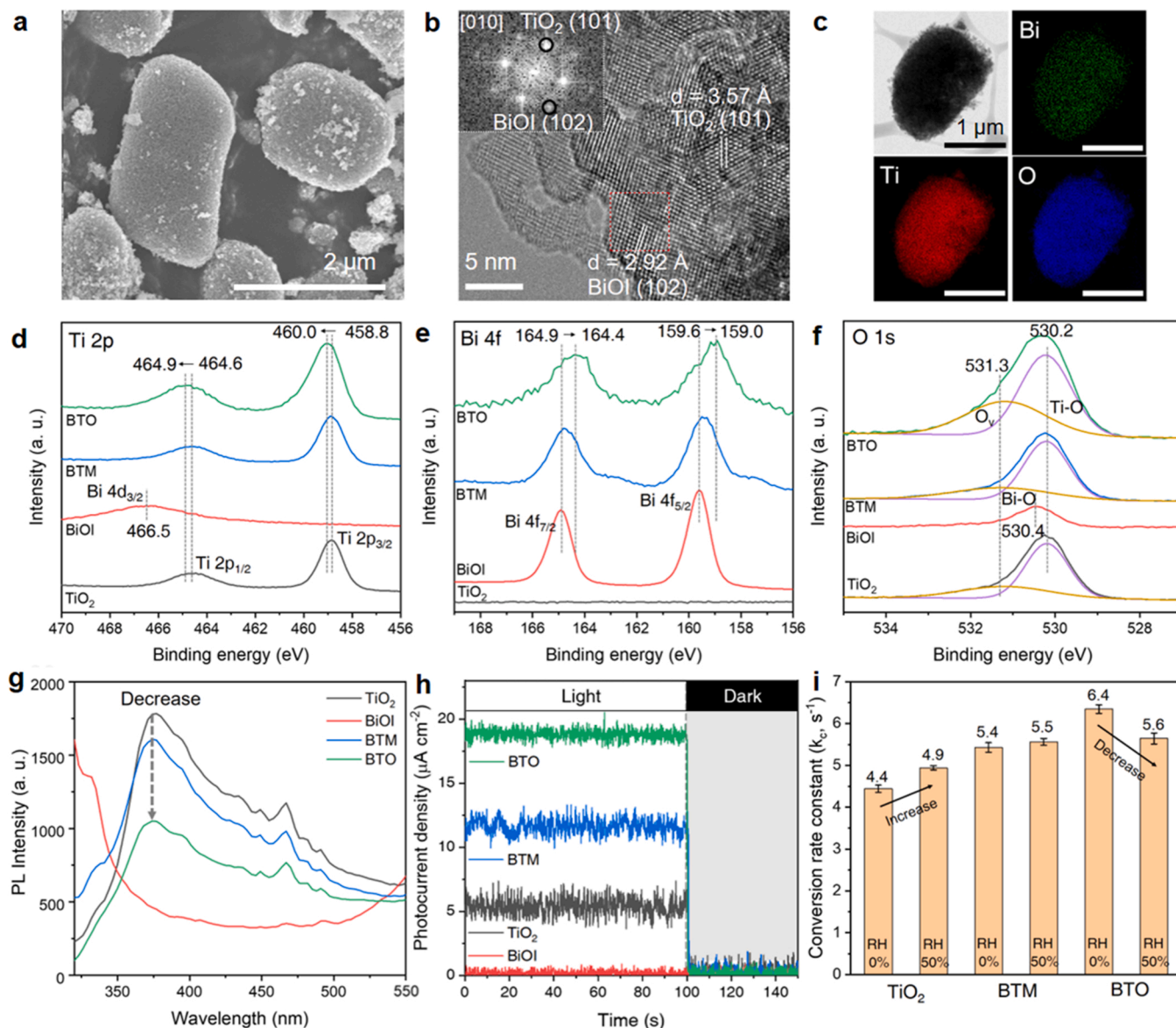
Fig. 1. (a) SEM image of BTO. Scale bar: 2 μm. (b) HR-TEM image and its FFT analysis of BTO. Scale bar: 5 nm. (c) STEM image of BTO and elemental mapping of Bi, Ti, and O elements. Scale bar: 1 μm. High-resolution XPS survey spectra of the TiO_2, BiOI, BTM and BTO; (d) Ti 2p, (e) Bi 4 f and (f) O 1 s (g) PL spectra of TiO_2, BiOI, BTM, and BTO under 310-nm excitation. (h) Photocurrent density of TiO_2, BiOI, BTM, and BTO under 365-nm UV irradiation at 0.5 V (vs. Ag/AgCl), (0.1 M phosphate buffer, pH 7) (i) HCHO-to-CO_2 photoconversion reaction rate constant (k_c) of TiO_2, BTM, and BTO under different RH conditions (20 ppmv HCHO in air balance, 500 ml min^{-1}, 365-nm UV LED).

separating photo-generated charge carriers in the BTO samples. Photo-electrochemical measurements were used to investigate the enhanced photocatalytic activity of BiOI/TiO_2 under UV light irradiation (Fig. 1 h). BTO showed a photocurrent density of 18.7 μA cm^{-2}, 3.7 times higher than TiO_2, demonstrating successful electron-hole separation in the composite. The photocurrent intensity of BTO is about 1.6 times higher than BTM, indicating better interfacial contact between BiOI and TiO_2 in BTO for charge transportation.

Photodegradation tests (365-nm irradiation) of gaseous HCHO by TiO_2, BTM, and BTO were performed in a single-pass reactor under different relative humidities (RH) (Fig. S6). We compared the HCHO-to-CO_2 conversion rate constants (k_c) of the photocatalysts using Equation (3). Pristine TiO_2 exhibited a k_c of 4.4 s^{-1} in dry air (RH 0 %) (Fig. 1i). We attribute the photodegradation activity of TiO_2 in the absence of humidity to water adsorbed on its large specific surface area (288 m^2 g^{-1}) [24]. Humid conditions (RH 50 %) facilitated TiO_2 activity. The BiOI/TiO_2 heterostructures demonstrated increased photodegradation

activity relative to TiO_2. In dry conditions, the BTO catalyst achieved the highest k_c of 6.4 s^{-1}, 1.5-fold higher than TiO_2. It suggests that catalyst photoactivity is closely related to the heterojunction. Interestingly, the photocatalytic degradation activity of BTO decreased with moisture introduction, contrary to previous studies on photocatalytic VOC degradation [25–27].

3.3. Radical monitoring

To investigate the phenomena observed under different humidity conditions, we focused on the ROS generation of the BTO photocatalyst. We compared the PL spectra of 2-hydroxyterephthalic acid (HTA) formed from the reaction of terephthalic acid (TA) with the •OH [28]. Fig. S7a show the PL peak intensity of HTA using different photocatalysts during the UV illumination. No PL signal is observed when the BiOI sample is irradiated, indicating no •OH production. In TiO_2, a gradual increase in PL intensity is observed with increasing irradiation

time, indicating the production of •OH originating from the attack of the photo-induced valence band (VB) hole on nucleophilic water [29]. However, PL decreases were observed in the BiOI/TiO$_2$ heterostructures. BTO exhibited relatively a low PL intensity compared to BTM. The results imply that •OH generation in BTO is suppressed by hole transfer from the VB of TiO$_2$ to the VB of BiOI induced by the built-in internal electric field of the p-n junction. The increased junctions between TiO$_2$ and BiOI in BTO promoted PL reduction.

We traced the major photo-generated ROS of BTO for HCHO photodegradation using applied EPR. ROS production signals corresponding to 5,5-Dimethyl-1-pyrroline N-oxide (DMPO)-•OH, DMPO-•O$_2^-$, and

2,2,6,6-tetramethylpiperidine (TEMP)-^{1}O$_2$ were observed under UV irradiation. As shown in Fig. 2a, •OH was generated only in TiO$_2$, consistent with the HTA detection results in Fig. S7. Characteristic •O$_2^-$ peaks were similarly detected in both TiO$_2$ and BTO (Fig. 2b). Fig. 2c shows that ^{1}O$_2$ was also detected in both photocatalysts. The ^{1}O$_2$ peak signal intensity is notably stronger in BTO than in TiO$_2$. EPR spectra showed that the main radical species in BTO were ^{1}O$_2$ and •O$_2^-$ rather than •OH.

This photo-induced ROS generation of BTO can be explained by band alignment. Mott–Schottky analysis yields the flat band potential of a semiconductor, representing its apparent Fermi level [30]. The results in
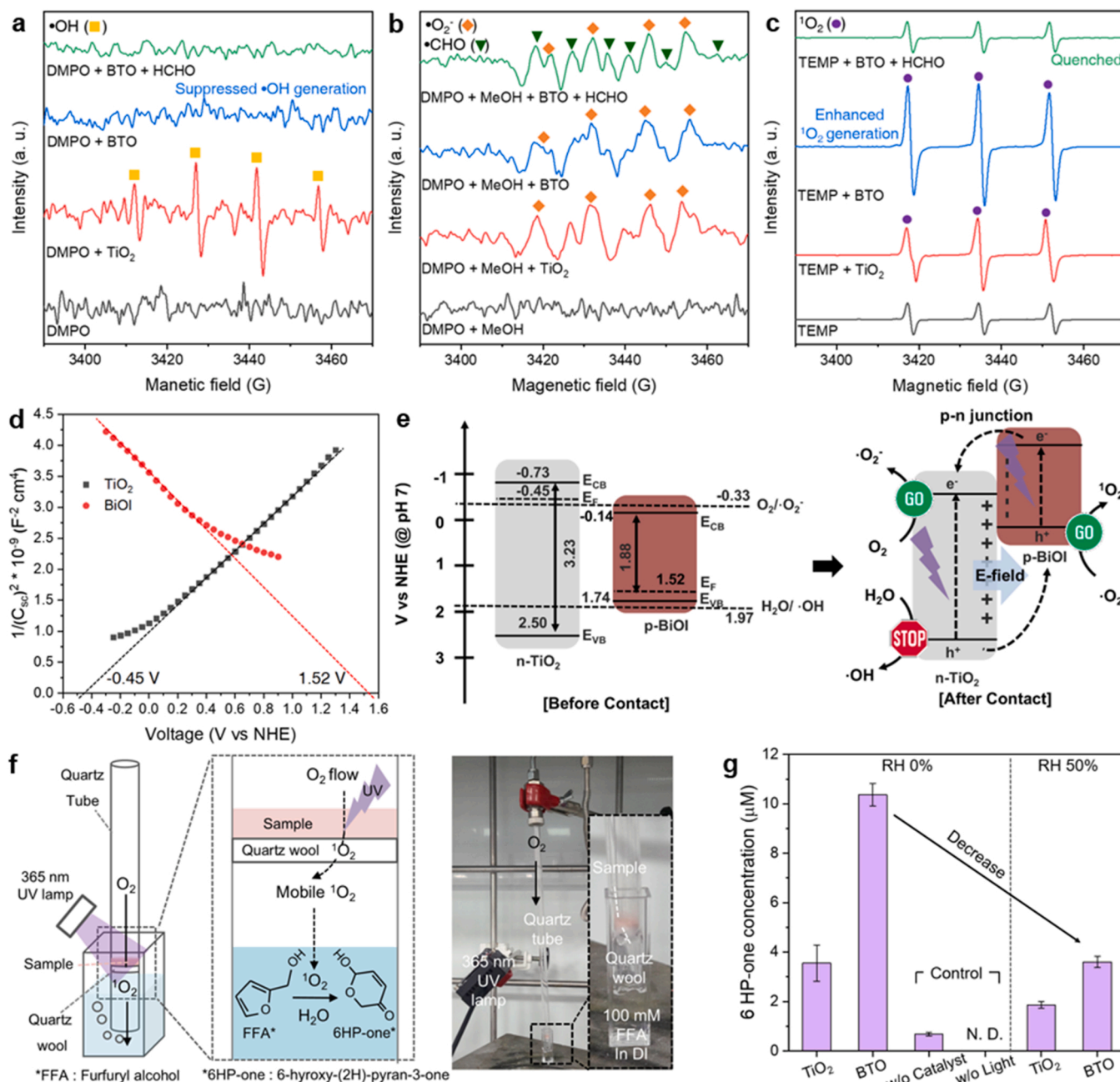

Fig. 2. EPR spectra of (a) DMPO-•OH, (b) DMPO-•O$_2^-$. For •O$_2^-$ detection, methanol was added into the solution to avoid the interference of •OH, and (c) TEMP-^{1}O$_2$ in solution with photocatalysts. The upper green spectra indicate the EPR analysis with the addition of aqueous HCHO. Hyperfine splitting constant: DMPO-•OH (α_N = 15 G, α_H = 14.8 G), DMPO-•O$_2^-$ (α_N = 14.7 G, α_H^β = 7.7 G), DMPO-•CHO (α_N = 12.5 G, α_H^β = 22.7 G), TEMP-^{1}O$_2$ (α_N = 17.2 G). (d), Mott–Schottky plots of TiO$_2$ and BiOI. (e) Band alignment of TiO$_2$ and BiOI and plausible reactions for photo-induced ROS generation after p-n heterojunction in BTO. (f) A schematic illustration and photograph of the in-situ experimental set-up for mobile ^{1}O$_2$ detection. FFA (100 μM) in DI water reacts with mobile ^{1}O$_2$ detection and converts to 6-HP-one. (G) Mobile ^{1}O$_2$ detected by the formation of 6-HP-one from the degradation of FFA.

Fig. 2d indicate that TiO_2 is an n-type semiconductor and BiOI is a p-type semiconductor [31]. Thus, BTO can be considered a p-n heterojunction structure. The Fermi level of TiO_2 and BiOI from the Mott–Schottky plot are − 0.45 and 1.52 V (vs. NHE, pH 7), respectively. The XPS-VB results of TiO_2 and BiOI were 2.95 and 0.22 eV, indicating the energy gap between the VB and the Fermi level (Fig. S8) [32]. Based on the Mott–Schottky, XPS-VB results, and band gap data, we estimated the energy band structure of the two semiconductors (Fig. 2e left). •OH generation is favored in TiO_2 because the VB level of TiO_2 is more positive than the $E(H_2O/•OH)$ of 1.97 V (vs. NHE, pH 7). When TiO_2 and BiOI are in contact, the Fermi level (E_F) should be at equilibrium, and a built-in internal electric field is formed at the p-n junction [33,34]. This electric field caused photo-excited electrons in the conduction band (CB) of BiOI to be transferred to that of TiO_2, while photo-generated holes in the VB of TiO_2 were transferred to that of BiOI. Consequently, •OH was not generated by BTO photocatalysts because the VB level of BiOI is more negative than $E(H_2O/•OH)$. The greater generation of $^1O_2$ in BTO than TiO_2 in the EPR spectra (Fig. 2c) reflects the accumulated holes in the VB of BiOI oxidizing •O_2^- to $^1O_2$. By quenching test using $^1O_2$ trapping chemical furfuryl alcohol (FFA), we verified the transformation of •O_2^- into $^1O_2$ by holes. $^1O_2$ generation was observed by FFA decrease in BTO dispersed aqueous solution. As shown in Fig. S9, BTO showed FFA reduction under UV light irradiation. However, after addition of hole scavenger TEOA, concentration of FFA was maintained after the reaction in BTO dispersed solution. The result of quenching test indicates that if holes were quenched there was no $^1O_2$ generation by BTO. In BTO, electrons accumulated in the CB of TiO_2 reduce O_2 to •O_2^-, and then the holes accumulated in the VB of BiOI oxidize •O_2^- to $^1O_2$ (Fig. 2e right).

We conducted EPR analyses with the addition of HCHO to identify radical intermediates formed when the ROS reacts with HCHO. After adding HCHO, the $^1O_2$ signal in BTO was quenched (Fig. 2c). However, the •O_2^- peak intensity was maintained, and a new •CHO radical intermediate simultaneously appeared (Fig. 2b). We considered that •O_2^- did not react with HCHO because its reactivity is known to be lower than other ROS [5]. In TiO_2, the signals of both •OH and $^1O_2$ were quenched due to reacting with HCHO, and the new •CHO peak was also observed along with •O_2^- (Fig. S10). These observations demonstrate that $^1O_2$ is the main ROS in BTO and oxidizes HCHO into •CHO during HCHO-to-CO_2 photoconversion. For TiO_2, the main ROS is •OH.

To confirm that $^1O_2$ was the major ROS utilized by the p-n junction photocatalyst BTO, we monitored mobile gas-phase $^1O_2$ with an experimental set-up (Fig. 2 f). The $^1O_2$ generated by photocatalytic reactions diffused in the gas phase as mobile $^1O_2$. Mobile $^1O_2$ arriving from the photocatalyst through O_2 gas flow chemically converts FFA in solution into 6-hydroxy-2 H-pyran-3(6 H)-one (6-HP-one) (Fig. S11). As shown in Fig. 2 g, BTO showed 3-fold greater production of mobile $^1O_2$ compared to TiO_2 under dry conditions. This reflects that the p-n junction photocatalyst BTO enhanced mobile $^1O_2$ generation compared to TiO_2. Since gaseous $^1O_2$ can diffuse freely towards a target gas due to its second-scale lifetime in dry air, it can be considered a dominant photooxygenation reactant [35,36]. The mobile $^1O_2$ generation in BTO can explain its high k_c in dry conditions in Fig. 1i. As control experiments, we conducted mobile $^1O_2$ analyses without a photocatalyst or light. These negative control experiments proved that mobile $^1O_2$ was generated from the photocatalyst under light irradiation. In humid conditions, the amount of $^1O_2$ generated by both photocatalysts decreased, attributable to the quenching of mobile $^1O_2$ by airborne H_2O [16]. Furthermore, H_2O can be adsorbed on the BTO surface competitively with O_2, causing low $^1O_2$ generation. The $^1O_2$ monitoring experiments prove that $^1O_2$ is the main ROS of the p-n junction photocatalyst and explain the negative effect of humidity on BTO photoconversion (Fig. 1i).

3.4. DFT calculations

We performed DFT calculations to elucidate the role of BiOI in $^1O_2$

generation (Details in Supplementary materials). Here, we used BiOI slab to model BTO catalyst instead of using explicit BiOI/TiO_2 slab, since the impact of supporting TiO_2 on the bonding nature of BiOI and $^1O_2$ was found to be negligible (Fig. S12). We selected (102) and (101) surfaces for BiOI and TiO_2, respectively, based on the XRD and HR-TEM data (Fig. S13). We found that surface termination with a Bi–I dangling bond is the most energetically favorable conformation for BiOI. Fig. 3a shows the free energies of two reaction pathways on the BiOI (102) surface: $^1O_2$ generation from •O_2^-, and •OH generation from H_2O. The $^1O_2$ production pathway is energetically downhill in free energy, which supports the finding that $^1O_2$ is actively produced by BTO. However, once adsorbed H_2O is converted to •OH, it is difficult to desorb from BiOI due to the large desorption energy (3.51 eV; Fig. 3a). Therefore, adsorbed •OH (*OH) blocks the BiOI active sites, inhibiting $^1O_2$ formation. Thus, the airborne moisture might suppress $^1O_2$ generation in BTO (Fig. 1i) by both $^1O_2$ quenching and active site blocking. For TiO_2, we studied the catalytic pathways on sub-surface O-vacancies (V_O) [37] because O_2 does not chemically interact with the bare surface without sub-surface vacancies (Fig. S14). In contrast to BiOI, there is a high free energy barrier (3.11 eV) for desorbing •O_2^- (*O_2) from TiO_2 (101) to produce $^1O_2$ (Fig. 3b). H_2O prefers to adsorb on the bare TiO_2 (101) surface and desorbs as •OH. This explains the much lower $^1O_2$ generation on TiO_2 compared to BTO in dry conditions (Fig. 2c, g).

To analyze the weaker chemical interaction of O_2 with BiOI than with TiO_2, we calculated the partial density of states (PDOS) for both. In Fig. 3c, the PDOS of the bare BiOI (102) surface with Bi–I dangling bonds does not contain any midgap surface states due to the shallow nature of I-vacancies [38]. Therefore, the highest occupied molecular orbital (HOMO) of the chemisorbed O_2 only interacts with the CB of BiOI (Fig. 3e). Thus, O_2 and BiOI form weak chemical interactions, which can be seen from the localized PDOS of O atoms near the Fermi level (E_F) (Fig. 3c, right panel). In contrast, the O-vacancy generates a midgap state in TiO_2 (Fig. 3d, left panel). This midgap state acts as a frontier orbital and interacts with the lowest unoccupied molecular orbital (LUMO) of O_2 and the interaction between HOMO of O_2 and CB of TiO_2 [39]. Thus, O_2 forms stronger chemical interactions with TiO_2 than BiOI, which can be seen from the hybridized O orbitals with Ti orbitals in the right panel of Fig. 3d (see Fig. 3f for a schematic illustration). The DFT findings explain the preferred reaction pathway for $^1O_2$ generation on the BTO photocatalyst; O_2 tends to adsorb on BiOI (102) and react with a hole in the valence bond, then easily desorbs as a mobile $^1O_2$. This supports our view that p-n photocatalyst BTO utilizes $^1O_2$ as a major ROS originating from O_2 rather than •OH.

3.5. The effect of $^1O_2$ generation on HCHO degradation

To determine whether $^1O_2$ generation by BTO creates oxidative conditions promoting HCHO degradation, in-situ DRIFTS analysis was employed. The spectral changes of the photocatalyst surface were observed under a series of sequential reaction conditions; (1) 60 min HCHO adsorption (Fig. 4a), (2) 60 min UV light irradiation with HCHO adsorption (Fig. 4b), and (3) 90 min UV light irradiation without HCHO (Fig. 4c). With the introduction of HCHO in step 1, peaks for dioxymethylene (DOM) species (peak 1; ν(C=O) 1112, 1150, 1174 cm^{-1}, ν(OCO) 1420 cm^{-1}) were measured, reflecting HCHO adsorbed on the catalyst surface and turned into DOM as a primary intermediate (Fig. 4a) [40].

In step 2, we compared HCHO photodegradation in BTO to that of TiO_2 in terms of oxidative conditions (Fig. 4b). The spectral changes of TiO_2 were firstly measured under dry conditions (RH 0 %, O_2 20 %) and then compared to less oxidative (RH 0 %, O_2 0 %; lack of O_2) and more oxidative conditions (RH 50 %, O_2 20 %; humidity supply). In TiO_2, DOM species (peak 1) disappear under UV irradiation in dry conditions. Instead, peaks consistent with monodentate formate (peak 2; ν_{as}(OCO) 1556, 1572 cm^{-1}) [41,42], monodentate carbonate (peak 3; ν_s(OCO) 1365 cm^{-1}) [43], and bidentate carbonate (peak 4; ν_s(OCO) 1310,
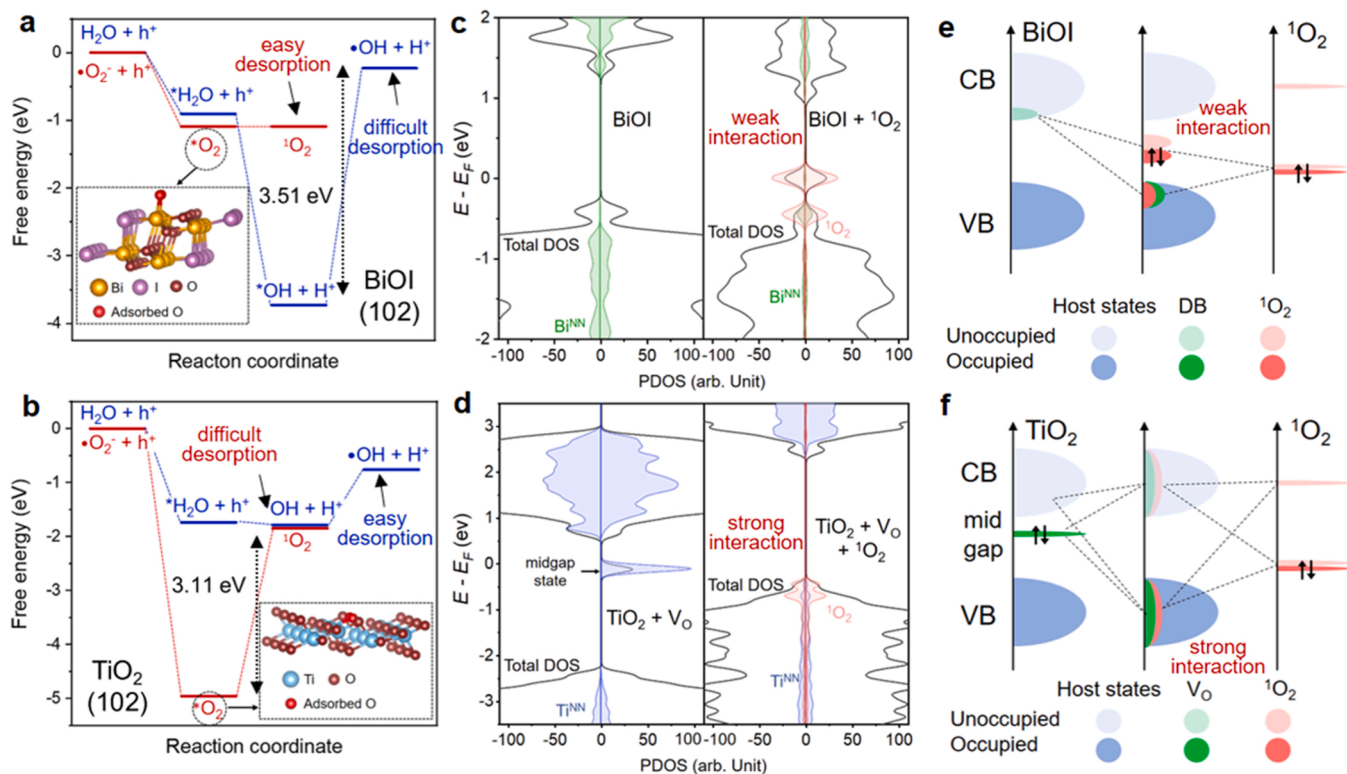
Fig. 3. The free energy diagrams of $^1O_2$ and •OH production on (a) BiOI and (b) TiO$_2$. The partial density of states (PDOS) of (c) BiOI and (d) TiO$_2$ without (left panel) and with (right panel) adsorption of O$_2$. Bi^{NN} indicates the nearest-neighbor Bi atom near the dangling bond, and Ti^{NN} indicates the nearest-neighbor Ti atoms around the vacancy. The PDOS of Bi, O, and Ti^{NN} are multiplied by 5 times. Schematic of chemical bonding of O$_2$ with (e) BiOI and (f) TiO$_2$.

ν(C=O) 1649 cm^{-1} [41] continually increase, indicating the accumulation of intermediates on the TiO$_2$ surface. Under the less oxidative condition (lack of O$_2$), however, the amount and rate of DOM conversion into formate and carbonate drastically decreased. Furthermore, the ratio of generated minor intermediates (by-products) such as bridged formate (peak 5; ν_s(OCO) 1377, ν_{as}(OCO) 1540 cm^{-1}) [44], bridged carbonate (peak 6; ν(C=O) 1672 cm^{-1}) [45], and bidentate bicarbonate (peak 7; ν(CO) 1290 cm^{-1}) [46] increased during HCHO photodegradation (Fig. 4d, e, Figs. S15 and S16). The lack of O$_2$ depressed ROS production of TiO$_2$, causing incomplete oxidation. The accumulation of these by-products might block the catalyst surface active sites, inhibiting HCHO photodegradation [42]. Under more oxidative conditions (humidity supply), the accumulation of formate and carbonate approached the steady state more rapidly, and fewer minor intermediates by-products were detected, indicating more ROS generation due to airborne H$_2$O. Interestingly, BTO under dry conditions showed DRIFTS spectra similar to those of TiO$_2$ under the more oxidative condition. The proportion of generated minor intermediates was lower than that of TiO$_2$ in dry and less oxidative conditions (Fig. 4d, e).

In step 3 of Fig. 4c, the HCHO was cut off after formate and bicarbonate intermediates accumulation reached their maximum concentration. The resulting spectra demonstrated the photodegradation of intermediates accumulated on the catalyst surface. The degradation kinetics of the intermediates fitted with a pseudo first-order correlation (Fig. 4 f, g). To compare the kinetics under different oxidation conditions, we calculated the photodegradation rate constant (k_d) (Equation (4)) [27]. The highest degradation rate was observed under the more oxidative condition on TiO$_2$. Under dry conditions, BTO showed higher k_d values for formate and carbonate decomposition than TiO$_2$ in dry and less oxidative conditions. It is well known that formate photodegradation is the rate-determining step in HCHO-to-CO$_2$ oxidation [47]; therefore, the 4.1-fold higher k_d value of BTO for formate photo-oxidation compared to TiO$_2$ under dry conditions (Fig. 4 f)

implies that BTO induces a more oxidative condition attributable to $^1O_2$ generation. In the absence of O$_2$, by-products accumulated on the BTO surface and were slowly degraded under UV light irradiation (Fig. S17). It confirms that the $^1O_2$-driven oxidative conditions created by BTO facilitate HCHO photoconversion without by-products even in dry conditions.

3.6. Reaction mechanism and application

Based on the results above, we propose a $^1O_2$-driven HCHO photodegradation mechanism on the BTO catalyst surface and gas-phase reaction. The p-n junction in BTO enables the transfer of photo-generated electrons and holes, which are accumulated in the CB of TiO$_2$ and VB of BiOI, respectively (Fig. 5a). •OH production is inhibited at the VB of TiO$_2$ in BTO, confirmed by EPR and PL spectra in Fig. 2a and Fig. S7. Gaseous O$_2$ reacts with accumulated photogenerated electrons and holes of BTO in order and turns into $^1O_2$ (Fig. 5a left), finally leading to HCHO photodegradation. Different possible photocatalytic degradation pathways with ROS may cause various intermediates (Fig. 5b). In the gas phase, mobile $^1O_2$ may react with gaseous HCHO via H-abstraction, forming a •CHO intermediate (Path 1) [47]. We experimentally proved that mobile $^1O_2$ is the major ROS of BTO in the gas phase and contributes to •CHO production (Fig. 2b, c). The •CHO intermediate was assumed to undergo coupling with $^1O_2$ by radical termination reactions to produce carbonate (bicarbonate) [41,47], which could be dissociated into CO$_2$ and H$_2$O [48]. To clarify Path 1, further studies about the monitoring gas-phase intermediates are needed. Alternatively, ROS may convert catalyst surface-absorbed HCHO into CO$_2$ (Path 2). in-situ DRIFTS analysis of intermediates on the BTO surface provided insights into in-situ reaction pathway. HCHO adsorbed on the catalyst as DOM is oxidized into formate (monodentate formate) under oxidative conditions induced by $^1O_2$. Formate undergoes dehydrogenation to carbonate (monodentate, bidentate carbonate) in the ROS oxidation process. The
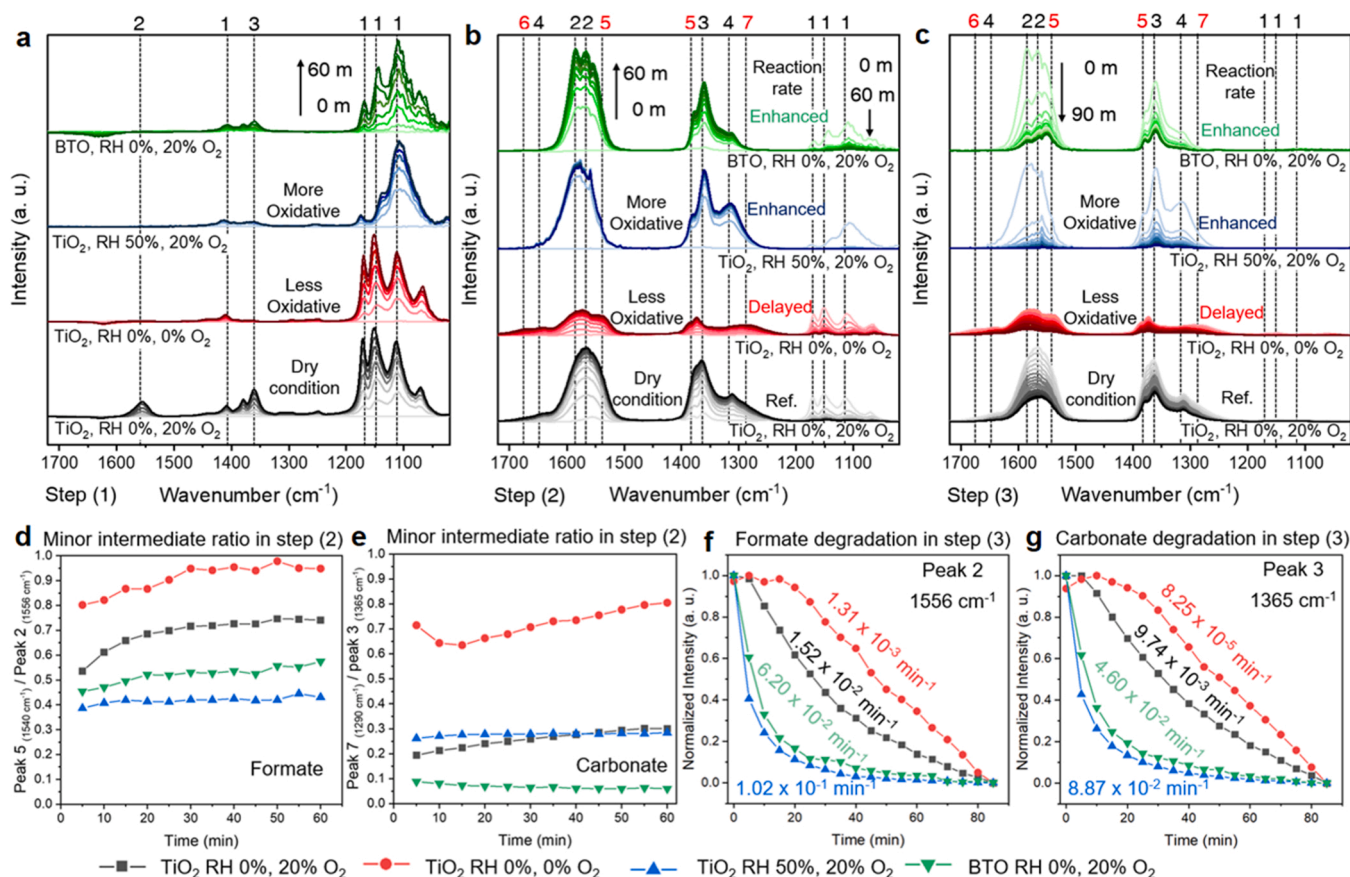
Fig. 4. In-situ DRIFTS spectra of photocatalysts for (a) step 1, i.e. HCHO adsorption (20 ppmv, N_2 balanced, 200 ml min^{-1}) under dark conditions for 60 min, followed by (b) step 2, i.e. UV light (365 nm) irradiation with HCHO adsorption for 60 min, and finally (c) step 3, i.e. UV light irradiation without HCHO after intermediate accumulation. The time interval between spectra is 5 min. Minor intermediate ratio of (d) formate (bridged formate/monodentate formate) and (e) carbonate (bidentate bicarbonate/monodentate carbonate) in step 2. Normalized intensity of (f) monodentate formate and (g) monodentate carbonate in step 3. Decomposition rate constants (k_d) of the photocatalysts under various oxidation conditions are also shown in the figure.

carbonate on the catalyst surface might be decomposed either by ROS or photo-generated holes. Notably, the accumulated holes on the VB can oxidize adsorbed organics directly instead of reacting with ROS [49]. Carbonate is reported to be a good hole scavenger [50]. Thus, accumulated holes in BTO might be consumed to oxidize carbonate species on the BTO surface into the final product CO_2.

Lastly, we employed the BTO for a photocatalytic filter for formaldehyde photodegradation to check the feasibility of air purification. The BTO was wash-coated on a honeycomb-type particulate filter monolith (Fig. 5c). We tested long-term HCHO photodegradation at the practical condition of RH 50 % under UV LED light irradiation in a single-pass reactor with a HCHO (20 ppmv) gas flow of 10 L min^{-1} (Fig. 5d and Fig. S18). Our photocatalytic filter exhibited 87 ± 1.3 % HCHO-to-CO_2 conversion efficiency for 150 h (Fig. 5e). We confirmed that the photocatalytic filter was not degraded by long-term operation and showed stable HCHO photoconversion, demonstrating a robust and sustainable HCHO photodegradation performance.

4. Conclusion

In summary, we have demonstrated a singlet oxygen-driven HCHO-to-CO_2 photodegradation via a BiOI/TiO_2 composite. The p-n junction in the composite inhibited charge recombination and enhanced its photocatalytic activity. The BTO catalyst showed a 1.5-times greater reaction rate constant than TiO_2. We used spectroscopic analyses and radical monitoring to validate that the rapid charge transfer in the p-n junction of BTO boosted mobile $^1O_2$ generation and suppressed •OH formation. The diffusion of mobile $^1O_2$ in the gas phase was confirmed by an

experimental set-up using the trapping chemical furfuryl alcohol (FFA). Furthermore, we provided a theoretical explanation for the energetically favorable $^1O_2$ generation pathway on the BTO surface by DFT calculation. Based on the results, we proposed a mechanism involving the reactive ROS and intermediates in gaseous HCHO photo-oxidation by BTO. Finally, we verified the BTO catalyst to HCHO photodegradation in a single-pass honeycomb-type filter. This work is the first example of a $^1O_2$-driven gaseous HCHO photodegradation. Our approach provides expanded new insights for gaseous HCHO photodegradation via mobile $^1O_2$.

CRediT authorship contribution statement

Su Keun Kuk: Conceptualization, Methodology, Investigation, Data processing, Writing – original draft. **Sang Min Ji:** Conceptualization, Investigation, Methodology. **Sungwoo Kang:** Computational simulation. **Dong Sik Yang:** Investigation. **Hyuk Jae Kwon:** Project administration, Supervision, Conceptualization. **Min Seok Koo:** Investigation. **Sehyeong Oh:** Computational simulation. **Hyun Chul Lee:** Project administration, Supervision, Conceptualization, Writing – review & editing.

Declaration of Competing Interest

The authors declare that they have no known competing financial interests or personal relationships that could have appeared to influence the work reported in this paper.
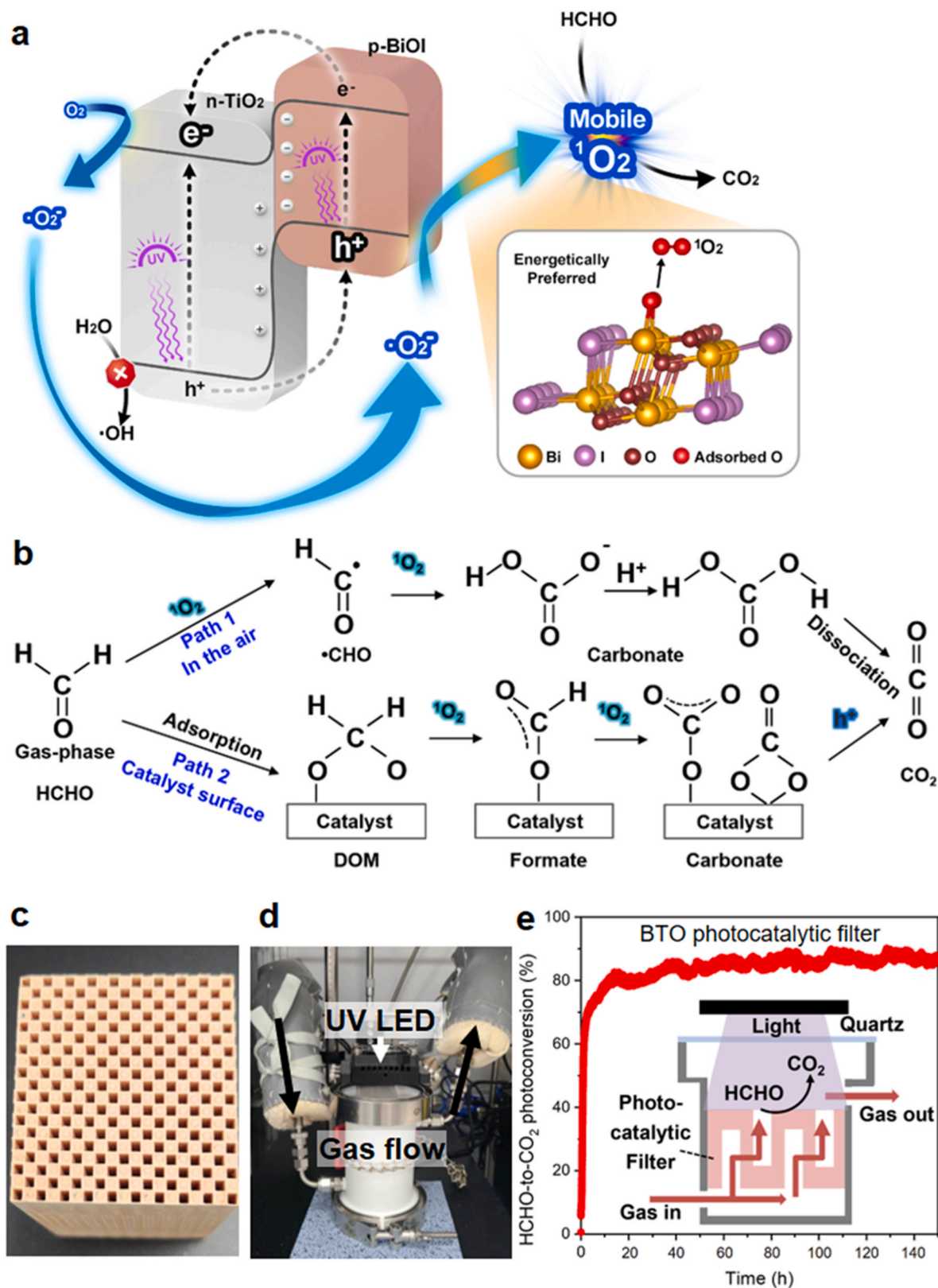
Fig. 5. (a) Scheme for $^1O_2$-driven photocatalytic degradation by p-n junction BTO. Charge transfer in the p-n junction of BTO induced generation of mobile $^1O_2$ generation instead of •OH. $^1O_2$ generation on BTO is more energetically favorable than •OH generation. Mobile $^1O_2$ accelerated gaseous HCHO photodegradation. (b) Schematic of the proposed reaction mechanistic pathways for HCHO photodegradation on BTO. Photographs of (c) BTO wash-coated photocatalytic filter (3.8 × 3.8 × 6 cm^3 ceramic filter 200 CPSI, BTO coating amount 43.6 g_{cat} L^{-1}), and (d) Experimental set-up of single-pass continuous flow reactor equipped with photocatalytic filter. (e) Long-term photocatalytic HCHO-to-CO_2 conversion by BTO coated photocatalytic filter (150 h). Inset shows a scheme for HCHO photodegradation by photocatalytic filter (20 ppmv HCHO in air balance, 10 L min^{-1}, Relative Humidity 50 %, 365-nm UV LED, 31 mW cm^{-2}).

Data availability

Data will be made available on request.

Appendix A. Supporting information

Supplementary data associated with this article can be found in the online version at doi:10.1016/j.apcatb.2023.122463.

References

[1] T. Vandyck, K. Keramidas, A. Kitous, J.V. Spadaro, R. Van Dinegen, M. Holland, B. Saveyn, Air quality co-benefits for human health and agriculture counterbalance costs to meet Paris Agreement pledges, Nat. Commun. 9 (2018) 4939.

[2] L. Mu, L. Liu, R. Niu, B. Zhao, J. Shi, Y. Li, M. Swanson, W. Scheider, J. Su, S.-H. Chang, S. Yu, Z.-F. Zhang, Indoor air pollution and risk of lung cancer among Chinese female non-smokers, Cancer Causes Control 24 (2013) 439–450.

[3] R. Li, Y. Huang, D. Zhu, W. Ho, J. Cao, S. Lee, Improved oxygen activation over a carbon/Co$_3$O$_4$ nanocomposite for efficient catalytic oxidation of formaldehyde at room temperature, Environ. Sci. Technol. 55 (2021) 4054–4063.

[4] Z. Shayegan, C.-S. Lee, F. Haghighat, TiO$_2$ photocatalyst for removal of volatile organic compounds in gas phase – a review, Chem. Eng. J. 334 (2018) 2408–2439.

[5] Y. Nosaka, A.Y. Nosaka, Generation and detection of reactive oxygen species in photocatalysis, Chem. Rev. 117 (17) (2017) 11302–11336.

[6] W. Zhao, M. Adeel, P. Zhang, P. Zhou, L. Huang, Y. Zhao, M.A. Ahmad, N. Shakoor, B. Lou, Y. Jiang, I. Lynch, Y. Rui, A critical review on surface-modified nano-catalyst application for the photocatalytic degradation of volatile organic compounds, Environ. Sci. Nano 9 (2022) 61–80.

[7] A. Carretero-Genevrier, C. Boissiere, L. Nicole, D. Grosso, Distance dependence of the photocatalytic efficiency of TiO$_2$ revealed by in situ ellipsometry, J. Am. Chem. Soc. 134 (2012) 10761–10764.

[8] M. Le Bechec, N. Costarramone, T. Pigot, S. Lacombe, Gas–phase photooxidation: reactors and materials, Chem. Eng. Technol. 39 (1) (2016) 26–38.

[9] F. Batault, F. Thevenet, V. Hequet, C. Rillard, L. Le Coq, N. Locoge, Acetaldehyde and acetic acid adsorption on TiO$_2$ under dry and humid conditions, Chem. Eng. J. 264 (2015) 197–210.

[10] X. Sun, C. Li, B. Yu, J. Wang, W. Wang, Removal of gaseous volatile organic compounds via vacuum ultraviolet photodegradation: review and prospect, J. Environ. Sci. 125 (2023) 427–442.

[11] Z. Shayegan, F. Haghighat, C.-S. Lee, Photocatalytic oxidation of volatile organic compounds for indoor environment applications: three different scaled setups, Chem. Eng. J. 357 (2019) 533–546.

[12] C. Schweitzer, R. Schmidt, Physical mechanisms of generation and deactivation of singlet oxygen, Chem. Rev. 103 (5) (2003) 1685–1758.

[13] K. Wang, S. Song, S. Jung, J. Hwang, M. Kim, J. Kim, J. Sung, J. Lee, Y. Kim, Lifetime and diffusion distance of singlet oxygen in air under everyday atmospheric conditions, Phys. Chem. Chem. Phys. 22 (2020) 21664–21671.

[14] J. Al-Nu'airat, I. Oluwoye, N. Zeinali, M. Altarawneh, B.Z. Dlugogorski, Review of chemical reactivity of singlet oxygen with organic fuels and contaminants, Chem. Rec. 21 (2) (2021) 315–342.

[15] N. Zeinali, I. Oluwoye, M. Altarawneh, B.Z. Dlugogorski, Destruction of dioxin and furan pollutants via electrophilic attack of singlet oxygen, Ecotoxicol. Environ. Saf. 184 (30) (2019), 109605.

[16] J. Lin, Q. Dai, H. Zhao, H. Cao, T. Wang, G. Wang, C. Chen, Photoinduced release of volatile organic compounds from fatty alcohols at the air–water interface: the role of singlet oxygen photosensitized by a carbonyl group, Environ. Sci. Technol. 55 (2021) 8683–8690.

[17] Q. Li, J. Zhao, H. Shang, Z. Ma, H. Cao, Y. Zhou, G. Li, D. Zhang, H. Li, Singlet oxygen and mobile hydroxyl radicals co-operating on gas–solid catalytic reaction interfaces for deeply oxidizing NOx, Environ. Sci. Technol. 56 (2022) 5830–5839.

[18] R. Zhou, J. Wu, J. Zhang, H. Tain, P. Liang, T. Zeng, P. Lu, J. Ren, T. Huang, X. Zhou, P. Sheng, Photocatalytic oxidation of gas-phase Hg^0 on the exposed reactive facets of BiOI/BiOIO$_3$ heterostructures, Appl. Catal. B. 204 (2017) 465–474.

[19] D. Wu, H. Wang, C. Li, J. Xia, X. Song, W. Huang, Photocatalytic self-cleaning properties of cotton fabrics functionalized with p-BiOI/n-TiO$_2$ heterojunction, Surf. Coat. Technol. 258 (2014) 672–676.

[20] S. Sultan, H. Lee, S. Park, M.M. Kim, A. Yoon, H. Choi, T.-H. Kong, I.-J. Koe, H.-S. Oh, Z. Lee, H. Kim, W. Kim, Y. Kwon, Interface rich CuO/Al$_2$CuO$_4$ surface for selective ethylene production from electrochemical CO$_2$ conversion, Energy Environ. Sci. 15 (2022) 2397–2409.

[21] J. Li, J. Zhong, Y. Si, S. Huang, L. Dou, M. Li, Y. Liu, J. Ding, Improved solar-driven photocatalytic performance of BiOI decorated TiO$_2$ benefiting from the separation properties of photo-induced charge carriers, Solid State Sci. 52 (2016) 106–111.

[22] X.H. Chen, X.L. Li, L.L. Wu, H.C. Fu, J. Luo, L. Shen, Q. Zhang, J.L. Lei, H.Q. Luo, N. B. Li, Nb$_2$O$_5$–Ni$_3$N heterojunction tuned by interface oxygen vacancy engineering for the enhancement of electrocatalytic hydrogen evolution activity, J. Mater. Chem. A. 9 (2021) 11563–11570.

[23] B. Li, X. Chen, T. Zhang, S. Jiang, G. Zhang, W. Wu, X. Ma, Photocatalytic selective hydroxylation of phenol to dihydroxybenzene by BiOI/TiO$_2$ p-n heterojunction photocatalysts for enhanced photocatalytic activity, Appl. Surf. Sci. 439 (2018) 1047–1056.

[24] A. Litke, Y. Su, I. Tranca, T. Weber, E.J.M. Hensen, J.P. Hofmann, Role of adsorbed water on charge carrier dynamics in photoexcited TiO$_2$, J. Phys. Chem. C 121 (2017) 7514–7524.

[25] X. Zhu, C. Jin, X.-S. Li, J.-L. Liu, Z.-G. Sun, C. Shi, X. Li, A.M. Zhu, Photocatalytic formaldehyde oxidation over plasmonic Au/TiO$_2$ under visible light: moisture indispensability and light enhancement. ACS Catal. 7 (10) (2017) 6514–6524.

[26] X. Zhu, D. Chang, X. Li, Z. Sun, X. Deng, A. Zhu, Inherent rate constants and humidity impact factors of anatase TiO$_2$ film in photocatalytic removal of formaldehyde from air, Chem. Eng. J. 279 (2015) 897–903.

[27] X.-Q. Deng, J. Liu, X. Li, B. Zhu, X. Zhu, A. Zhu, Kinetic study on visible-light photocatalytic removal of formaldehyde from air over plasmonic Au/TiO$_2$, Catal. Today 281 (2017) 630–635.

[28] J. Yu, S. Wang, J. Low, W. Xiao, Enhanced photocatalytic performance of direct Z-scheme g-C$_3$N$_4$–TiO$_2$ photocatalysts for the decomposition of formaldehyde in air, Phys. Chem. Chem. Phys. 15 (2013) 16883–16890.

[29] Y. Nosaka, A. Nosaka, Understanding hydroxyl radical (•OH) generation processes in photocatalysis, ACS Energy Lett. 1 (2016) 356–359.

[30] T.-F. Yeh, F.-F. Chan, C.-T. Hsieh, H. Teng, Understanding hydroxyl radical (•OH) generation processes in photocatalysis, J. Phys. Chem. C 115 (2011) 22587–22597.

[31] N. Sedaghati, A. Habibi-Yangjeh, M. Pirhashemi, S. Vadivel, Boosted visible-light photocatalytic performance of TiO$_{2-x}$ decorated by BiOI and AgBr nanoparticles, J. Photochem. Photobiol. A. 384 (2019), 112066.

[32] R.L.Z. Hoye, L.C. Lee, R.C. Kurchin, T.N. Huq, K.H.L. Zhang, M. Sponseller, L. Nienhaus, R.E. Brandt, J. Jean, J.A. Polizzotti, A. Kursumović, M.G. Bawendi, V. Bulović, V. Stevanović, T. Buonassisi, J.L. MacManus-Driscoll, Strongly enhanced photovoltaic performance and defect physics of air–stable bismuth oxyiodide (BiOI), Adv. Mater. 29 (36) (2017) 1702176.

[33] Y. Zhang, A. Sun, M. Xiong, D.K. Macharia, J. Liu, Z. Chen, M. Li, L. Zhang, TiO$_2$/BiOI p-n junction-decorated carbon fibers as weavable photocatalyst with UV–vis photoresponsive for efficiently degrading various pollutants, Chem. Eng. J. 415 (2021), 129019.

[34] P. Zhou, J. Yu, M. Jaroniec, All–solid–state Z–scheme photocatalytic systems, Adv. Mater. 26 (29) (2014) 4920–4935.

[35] A.M. Durantini, A. Greer, Interparticle delivery and detection of volatile singlet oxygen at air/solid interfaces, Environ. Sci. Technol. 55 (6) (2021) 3559–3567.

[36] C. Cantau, T. Pigot, R. Brown, P. Mocho, M.T. Maurette, F. Benoit-Marque, S. Lacombe, Photooxidation of dimethylsulfide in the gas phase: a comparison between TiO$_2$–silica and photosensitizer-silica based materials, Appl. Catal. B. 65 (2006) 77–85.

[37] M. Setvin, U. Aschauer, P. Scheiber, Y.-F. Li, W. Hou, M. Schmid, A. Selloni, U. Diebold, Reaction of O$_2$ with Subsurface Oxygen Vacancies on TiO$_2$ Anatase (101), Science 341 (6149) (2013) 988–991.

[38] H. Jin, E. Debroye, M. Keshavarz, I.G. Scheblykin, M.B.J. Roeffaers, J. Hofkens, J. A. Steele, It's a trap! On the nature of localised states and charge trapping in lead halide perovskites, Mater. Horiz. 7 (2020) 397–410.

[39] N. Hamamoto, T. Tatsumi, M. Takao, T. Toyao, Y. Hinuma, K. Shimizu, T. Kamachi, Effect of oxygen vacancies on adsorption of small molecules on anatase and rutile TiO$_2$ surfaces: a frontier orbital approach, J. Phys. Chem. C 125 (7) (2021) 3827–3844.

[40] X. Chen, G. He, Y. Li, M. Chen, X. Qin, C. Zhang, H. He, Identification of a facile pathway for Dioxymethylene conversion to formate catalyzed by surface hydroxyl on TiO$_2$-based catalyst, ACS Catal. 10 (2020) 9706–9715.

[41] S. Zhang, Y. Zhuo, C.I. Ezugwu, C.C. Wang, C. Li, S. Liu, Synergetic molecular oxygen activation and catalytic oxidation of formaldehyde over defective MIL-88B (Fe) nanorods at room temperature, Environ. Sci. Technol. 55 (12) (2021) 8341–8350.

[42] X. Li, H. Li, Y. Huang, J. Cao, T. Huang, R. Li, Q. Zhang, S. Lee, W. Ho, Exploring the photocatalytic conversion mechanism of gaseous formaldehyde degradation on TiO$_{2-x}$-OV surface, J. Hazard. Mater. 424 (2022), 127217.

[43] D.-Z. Zhao, C. Shi, X.-S. Li, A.-M. Zhu, B.W.-L. Jang, Enhanced effect of water vapor on complete oxidation of formaldehyde in air with ozone over MnOx catalysts at room temperature, J. Hazard. Mater. 239–240 (2012) 362–369.

[44] M. Chen, H. Wang, X. Chen, F. Wang, X. Qin, C. Zhang, H. He, High-performance of Cu-TiO$_2$ for photocatalytic oxidation of formaldehyde under visible light and the mechanism study, Chem. Eng. J. 390 (2020), 124481.

[45] H. Du, C.T. Williams, A.D. Ebner, J.A. Ritter, In Situ FTIR spectroscopic analysis of carbonate transformations during adsorption and desorption of CO$_2$ in K-promoted HTlc, Chem. Mater. 22 (11) (2010) 3519–3526.

[46] H. Li, X. Jiao, L. Li, N. Zhao, F. Xiao, W. Wei, Y. Sun, B. Zhang, Synthesis of glycerol carbonate by direct carbonylation of glycerol with CO$_2$ over solid catalysts derived from Zn/Al/La and Zn/Al/La/M (M = Li, Mg and Zr) hydrotalcites, Catal. Sci. Technol. 5 (2015) 989–1005.

[47] J. Yang, D. Li, Z. Zhang, Q. Li, H. Wang, A study of the photocatalytic oxidation of formaldehyde on Pt/Fe$_2$O$_3$/TiO$_2$, J. Photochem. Photobiol. A. 137 (2000) 197–202.

[48] S. Ghoshal, M.K. Hazra, H$_2$CO$_3$ → CO$_2$ + H$_2$O decomposition in the presence of H$_2$O, HCOOH, CH$_3$COOH, H$_2$SO$_4$ and HO$_2$ radical: instability of the gas-phase

H$_2$CO$_3$ molecule in the troposphere and lower stratosphere, RSC Adv. 5 (2015) 17623–17635.

[49] H. Belhadj, S. Hamid, P.K.J. Robertson, D.W. Bahnemann, Mechanisms of simultaneous hydrogen production and formaldehyde oxidation in H$_2$O and D$_2$O over platinized TiO$_2$, ACS Catal. 7 (2017) 4753–4758.

[50] N.M. Dimitrijevic, B.K. Vijayan, O.G. Poluektov, T. Rajh, K.A. Gray, H. He, P. Zapol, Role of water and carbonates in photocatalytic transformation of CO$_2$ to CH$_4$ on Titania, J. Am. Chem. Soc. 133 (11) (2011) 3964–3971.